Supporting Information for "Lattice dynamics of the polar orthorhombic phase of HfO$_2$"

Shiyu Fan,[1,2] Sobhit Singh,[1,3] Xianghan Xu,[3,4] Kiman Park,[5] Yubo Qi,[3] S. W. Cheong,[3,4] David Vanderbilt,[3] Karin M. Rabe,[3] and J. L. Musfeldt[5,2]

[1] *These authors contributed equally to this work*

[2] *Department of Physics and Astronomy,*

University of Tennessee, Knoxville, Tennessee, 37996, USA

[3] *Department of Physics and Astronomy,*

*Rutgers University, Piscataway, New Jersey 08854, USA*

[4] *Rutgers Center for Emergent Materials,*

Rutgers University, Piscataway, New Jersey 08854, USA

[5] *Department of Chemistry, University of Tennessee, Knoxville, Tennessee, 37996, USA*

Simulating the effect of the Yttrium substitution on the lattice dynamics

In order to investigate the role of Y substitution on the lattice dynamics of cubic (c) HfO$_2$, we performed additional DFT calculations on supercell structures having Y$_2$Hf$_6$O$_{15}$ composition. This composition corresponds to 25% Y substitution on the Hf sites, which is close to the HfO$_2$:20%Y as in our experiments. We start with a DFT optimized 8-formula unit (f.u.) supercell of pure c-HfO$_2$, and then systematically substitute two Hf atoms by two Y atoms and create an oxygen vacancy to maintain the charge neutrality, thus yielding Y$_2$Hf$_6$O$_{15}$ composition. We note that there are $^8C_2 = 28$ possible ways to distribute two Y atoms at eight Hf sites. Further, there are $^{16}C_1 = 16$ possible ways to distribute one oxygen vacancy at sixteen oxygen sites in the c phase. Thus, a total of $28 \times 16 = 448$ atomic configurations are possible for the Y$_2$Hf$_6$O$_{15}$ composition. We further utilize the crystal symmetry operations to remove the symmetrically equivalent supercells. All these supercells were generated using the SUPERCELL program.[S1] Lastly, we fully optimize all the generated supercells using the DFT convergence parameters as detailed in the main text, and select the lowest energy ground state configuration for further analyses.

The lowest energy structure of Y$_2$Hf$_6$O$_{15}$ is shown in Figure S1a. The calculated phonon spectrum of this structure, shown in Figure S1b, reveals the dynamical stability of this structure. We use the calculated phonon eigenvectors at the zone center to compute the infrared response of this system. The calculated infrared spectrum of Y$_2$Hf$_6$O$_{15}$, shown in Figure S1c, reveals a number of additional excitations - in addition to the fundamental T$_{1u}$ vibrational mode of cubic hafnia - that are being activated by Y incorporation and local symmetry breaking. Some of these additional features are predicted to be more intense than the T$_{1u}$ mode - in good agreement with the findings discussed in the main text. Analysis of the projected phonon density of states (PDOS) plot, shown in Figure S1d, suggests that the modes below 450 cm^{-1} have some contributions from the Y sublattice and Y-O bonds. We note that our simulations do not include the weak metallic background, which, in addition to the role of Y, may also have some contributions in the measured reflectance spectrum.
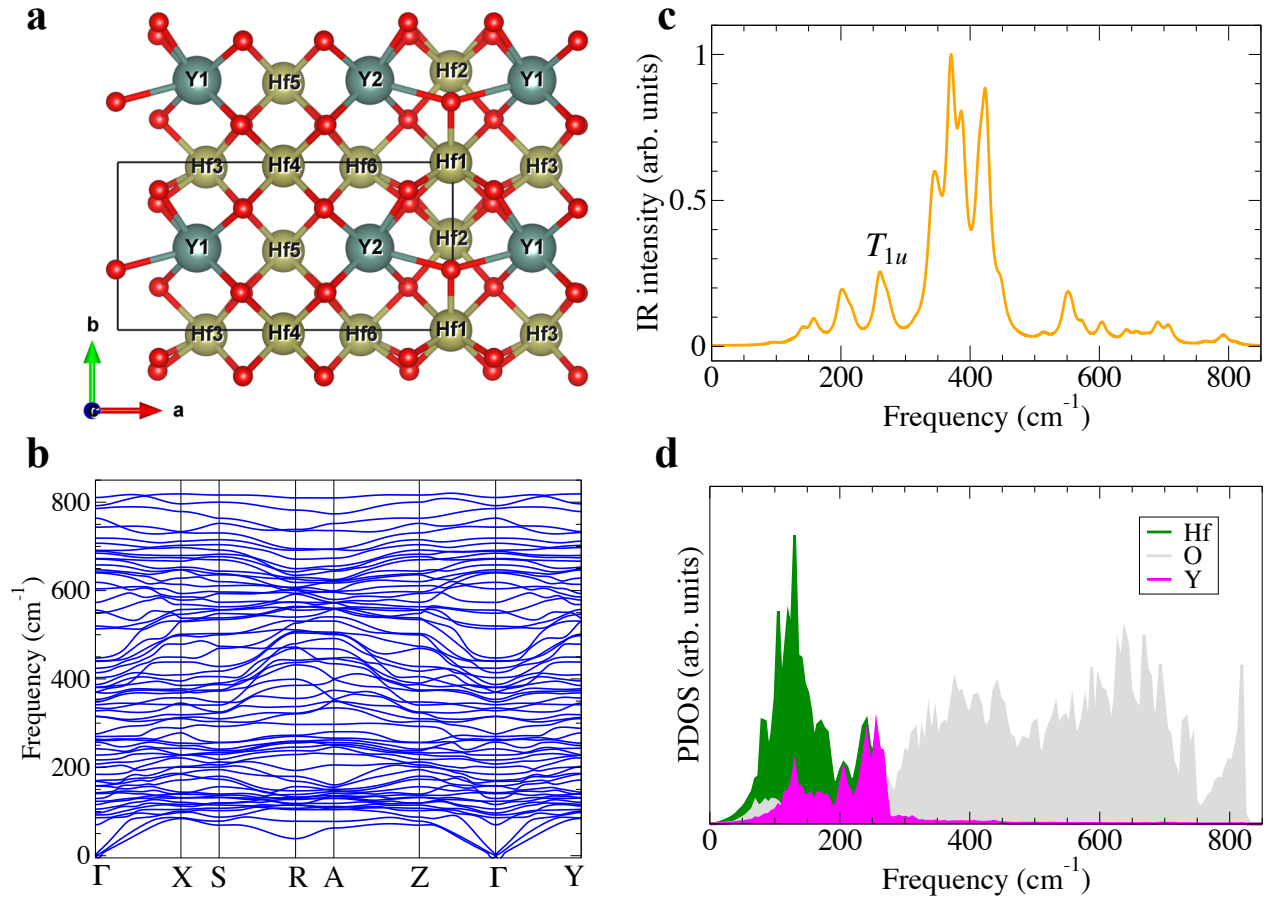
Supplementary Figure 1. **a,** The lowest energy crystal structure of $Y_2Hf_6O_{15}$ obtained after 25% Y substitution on Hf sites in an 8-f.u. cell of cubic hafnia. **b,** Calculated phonon dispersion, **c,** infrared (IR) spectrum, and **d,** projected phonon density of states (PDOS) for the structure shown in **a**.

Temperature dependence of phonon properties of the HfO$_2$:12%Y crystals

Figure S2 displays the infrared and Raman spectra of HfO$_2$:12%Y at both 300 K and base temperature (7 and 4 K). Data are shown for crystals with both in- and out-of-plane ferroelectric polarizations. Overall, the vibrational response depends only weakly on temperature, probably because the overall energy scale (for instance, given by the melting point) is so high in hafnia. That said, some of the phonon modes become sharper and better resolved at low temperature. This additional detail doesn't really reveal any new features; it mainly serves to confirm what is already evident at 300 K. In the infrared reflectance, the weak metallic background is still present, and in the Raman scattering response, the fluorescent background has similar character over the full temperature range.
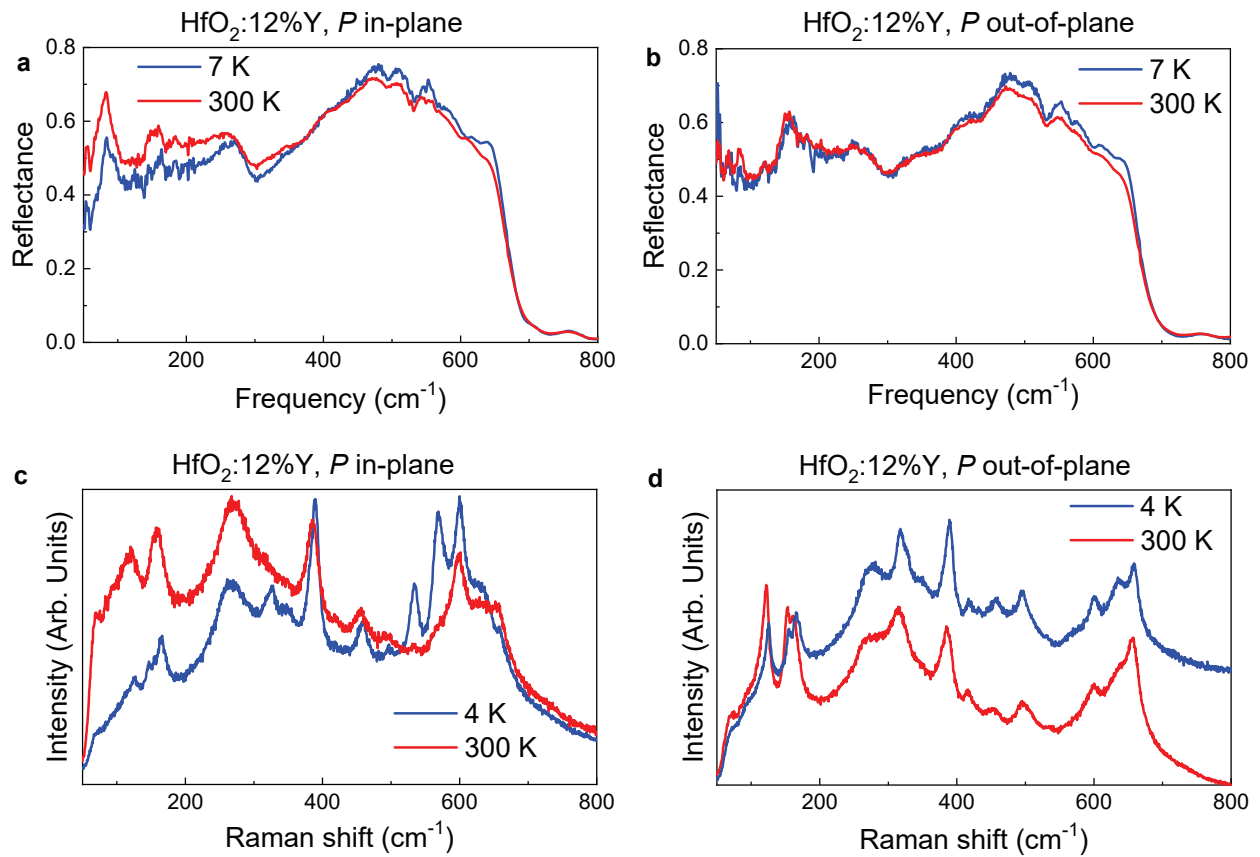
Supplementary Figure 2. **a,b,** Infrared reflectance of HfO$_2$:12% Y for samples with in- and out-of-plane spontaneous ferroelectric polarization measured at 7 and 300 K. **c,d,** Raman scattering spectra of HfO$_2$:12% for crystals with in- and out-of-plane spontaneous ferroelectric polarization measured at 4 and 300 K.
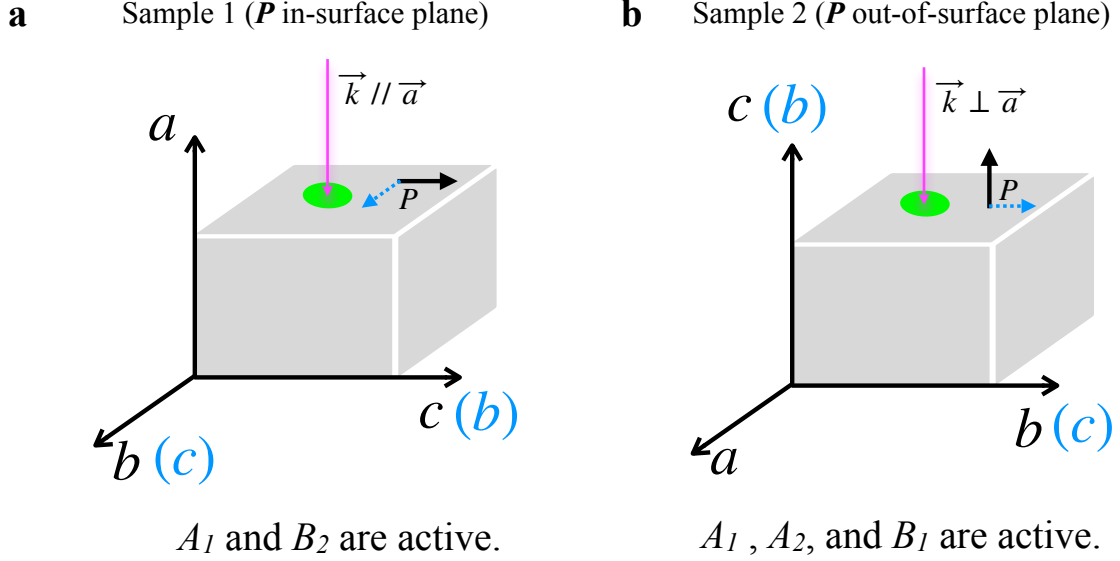
Measurement geometry of the HfO$_2$:12%Y

In order to experimentally detect all of the predicted Raman-active phonons in the orthorhombic-polar (*o-III*) phase of hafnia, we prepared two different HfO$_2$:12%Y samples having distinct surface orientations with respect to the direction of the spontaneous ferroelectric polarization ($\boldsymbol{P} \parallel \vec{c}$). In sample 1, referred as $\boldsymbol{P}$ in-surface plane, the surface is cut parallel to the direction of $\boldsymbol{P}$, whereas in sample 2, referred as $\boldsymbol{P}$ out-of-surface plane, the surface is cut perpendicular to the direction of $\boldsymbol{P}$. However, because of the strong mixing of the b and c lattice vectors due to twinning, we are not able to distinguish between the b and c axes. Therefore, in sample 2 we probe the combined ab- and ac-plane responses, whereas in sample 1 we probe the bc-plane response. It is worth noting that in sample 2 roughly 50% of the total $\boldsymbol{P}$ is out-of-the-surface plane while the other 50% of total $\boldsymbol{P}$ lies within the surface plane. Figure S3 displays schematics showing how samples with both in- and out-of-surface plane $\boldsymbol{P}$ were positioned for Raman scattering measurements, which were performed in the back-scattering geometry using unpolarized light.

Table I contains details of all infrared- and Raman-active phonons along with their Raman selection rules in the *o-III* phase of hafnia. The A$_1$ and B$_2$ symmetry modes are Raman active in sample 1, i.e., $\boldsymbol{P}$ in-surface plane sample, and the A$_1$, A$_2$, and B$_1$ symmetry modes are Raman active in sample 2, i.e., $\boldsymbol{P}$ out-of-surface plane sample. We note that the B$_1$ symmetry mode is Raman active in sample 2 only because of the mixing of the b and c axes due to twinning.

Supplementary Table I. **A summary of the infrared- and Raman-active phonon modes along with their Raman selection rules (unpolarized light) in the *o-III* phase of hafnia.**

Mode symmetry	Basis functions	Infrared activity	Raman activity in the back-scattering geometry
A_1	z, x^2, y^2, z^2	active	active in both samples ($\boldsymbol{k} \parallel \vec{a}$ and $\boldsymbol{k} \parallel \vec{c}$)
A_2	xy	inactive	active in the out-of-surface plane P sample ($\boldsymbol{k} \parallel \vec{c}$)
B_1	x, xz	active	active in the out-of-surface plane P sample ($\boldsymbol{k} \parallel \vec{b}$)
B_2	y, yz	active	active in the in-surface plane P sample ($\boldsymbol{k} \parallel \vec{a}$)

a   Sample 1 (**P** in-surface plane)   **b**   Sample 2 (**P** out-of-surface plane)

A_1 and B_2 are active. A_1, A_2, and B_1 are active.

Supplementary Figure 3. **a,** A schematic view of the Raman back-scattering measurement geometry for HfO_2:12%Y sample 1 having spontaneous ferroelectric polarization (**P**) within the surface plane, i.e., bc-plane. The wave vector (**k**) of the incoming and scattered light is parallel to the $\vec{a}$ lattice vector. **b,** A schematic view of the Raman back-scattering measurement geometry for HfO_2:12%Y sample 2 having (**P**) out-of-the-surface plane, i.e., ab- or ac-plane. The wave vector (**k**) of the incoming and scattered light is perpendicular to the $\vec{a}$ lattice vector. Note that the b and c axes are heavily mixed due to twinning. **P** is always parallel to the c axis. Dashed arrow denotes the orientation of **P** for the alternative configuration of the b and c axes (shown in blue).

Infrared and Raman spectra of the HfO_2:8%Y material

Figure S4 displays the infrared and Raman spectra of HfO_2:8%Y. This compound has mixed orthorhombic-antipolar and monoclinic phases, which makes our analysis challenging. Compared to the response of the pure orthorhombic-antipolar material with 11% Y [Fig. 2c], the metallic background is noticeably reduced in HfO_2:8%Y. It has not, however, diminished fully as can be seen by comparing these results with the infrared reflectance spectrum of the monoclinic sample (with 0% Y). As a result, the infrared-active phonons in HfO_2:8%Y are more prominent and less screened than those in the 11% material. Turning to the Raman response, the fluorescence background is again present in HfO_2:8%Y, although it is smaller than that in the pure orthorhombic-antipolar phase material (11% Y). This suggests that both metallicity and the fluorescence background decrease with diminishing Y incorporation

in this series of materials. The experimental results show an overall good match with the calculated phonons of the orthorhombic-antipolar phase, although some monoclinic peaks are observed in both infrared and Raman spectra as expected. One example is the B_g symmetry feature near 780 cm^{-1} in the Raman spectrum, which is a unique signature of the monoclinic phase [Fig. 4 and Table S1]. The temperature dependence of the vibrational response of HfO$_2$:8%Y is weak, similar to that in the 12% Y compound [Fig. S2]. Again, this is due to the overall high energy scales in this family of materials.
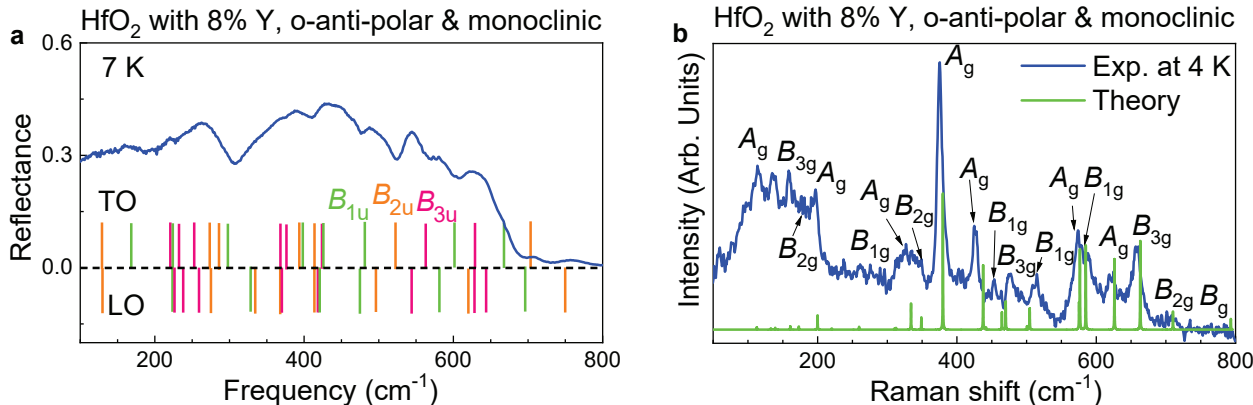
Supplementary Figure 4. **a,** Infrared reflectance spectra of the HfO$_2$: %8Y measured at 7 K, compared with the theoretically calculated infrared TO and LO peak positions in the pure *o-antipolar (o-AP)* phase. **b,** Raman spectra of the HfO$_2$: 8%Y measured at 4 K, compared with the calculated Raman spectrum of the orthorhombic antipolar phase of pure hafnia.

Vibrational fingerprints of the five different phases of hafnia

In Fig. 4 of the main text, we summarize the characteristic infrared- and Raman-active modes of the different phases of hafnia in a graphical form. Here, we identify the unique vibrational features of each phase in tabular form [Table S2], with the goal of making it easy to use the phonon pattern as a fingerprint for experimental determination of each phase. These distinguishing characteristics will be especially useful for the tetragonal system which has not yet been made in single crystal form. The distinguishing features of each phase will also make hafnia easier to identify as part of a mixture, composite, or superlattice.

Supplementary Table II. **The calculated phonon frequencies (in cm^{-1} units) useful for the identification of different phases of pure hafnia**

HfO$_2$: x%Y crystals	phase	polarization	Characteristic infrared modes	Characteristic Raman modes
20%	cubic	nonpolar	T$_{1u}$: 266	T$_{2g}$: 599
12%	orthorhombic	polar	A$_1$: 167 and 471 B$_1$: 497 and 643	A$_1$: 354, 396, and 471 B$_2$: 532 and 562
11%	orthorhombic	antipolar	B$_{3u}$: 187, 201, and 223 B$_{2u}$: 385 B$_{1u}$: 390, 485, and 622	A$_g$: 200, 380, and 438 B$_{2g}$: 710
0%	monoclinic	nonpolar	B$_u$: 330 and 518 A$_u$: 508 and 607	A$_g$: 500 B$_g$: 518 and 780
Not yet grown in single crystal form	tetragonal	nonpolar	A$_{2u}$: 321 E$_u$: 129	A$_{1g}$: 276 E$_g$: 677

Phonon displacement patterns of the B$_2$ and A$_1$ vibrational modes

Animations of the phonon displacement patterns of the B$_2$ mode at 252 cm^{-1} and A$_1$ mode at 354 cm^{-1} in gif format are attached to this Supplemental Information as separate files.

Born effective charges calculated for different phases of HfO$_2$

Table III contains the Born effective charges ($\mathbf{Z}^*$) for the independent atoms in the primitive cell of the five studied phases of bulk HfO$_2$. In each case, the $\mathbf{Z}^*$ is well above the Madelung limit. These results are in good agreement with the previous data reported for cubic, tetragonal, and monoclinic phases of hafnia.[S2]

Supplementary Table III. **Born effective charges (Z^*) for the independent atoms in the primitive cell of HfO$_2$ calculated using DFT (PBEsol).**

Z^*		cubic ($Fm\bar{3}m$)	tetragonal ($P4_2/nmc$)	o-III ($Pca2_1$)	o-AP ($Pbca$)	monoclinic ($P2_1/c$)
	xx	5.56	5.54	5.21	4.97	5.35
	xy	0.00	0.00	-0.02	-0.26	-0.39
	xz	0.00	0.00	0.05	0.03	0.21
	yx	0.00	0.00	-0.37	-0.05	-0.15
Hf	yy	5.56	5.54	5.49	5.46	5.30
	yz	0.00	0.00	0.14	0.39	-0.18
	zx	0.00	0.00	-0.04	0.12	-0.22
	zy	0.00	0.00	0.23	0.02	-0.36
	zz	5.56	5.01	5.01	5.30	4.83
	xx	-2.78	-3.33	-2.51	-2.46	-2.96
	xy	0.00	0.00	0.97	-0.58	-1.05
	xz	0.00	0.00	0.32	0.33	0.21
	yx	0.00	0.00	0.77	-0.64	-1.29
O$_1$	yy	-2.78	-2.21	-2.96	-2.96	-2.58
	yz	0.00	0.00	0.68	-0.79	-0.66
	zx	0.00	0.00	0.33	0.33	0.18
	zy	0.00	0.00	0.63	-0.97	-0.67
	zz	-2.78	-2.50	-2.50	-2.55	-2.28
	xx	-2.78	-3.33	-2.70	-2.51	-2.39
	xy	0.00	0.00	-0.15	-0.03	-0.10
	xz	0.00	0.00	-0.26	-0.33	-0.01
	yx	0.00	0.00	-0.08	-0.08	-0.16
O$_2$	yy	-2.78	-2.21	-2.53	-2.51	-2.72
	yz	0.00	0.00	-0.15	0.05	0.35
	zx	0.00	0.00	-0.29	0.29	0.04
	zy	0.00	0.00	-0.11	0.02	0.42
	zz	-2.78	-2.50	-2.51	-2.75	-2.55

DFT (PBEsol) optimized lattice parameters of different phases of HfO$_2$

Supplementary Table IV. DFT (PBEsol) optimized lattice parameters of different phases of HfO$_2$

Phase	Cell parameters	Cell angles (Å)	Experiment
Cubic	$a = b = c = 3.547$ Å	$\alpha = \beta = \gamma = 60°$	$a = b = c = 3.592$ Å (Ref. [S3])
Tetragonal	$a = b = 3.548$, $c = 5.102$ Å	$\alpha = \beta = \gamma = 90°$	–
o-III	$a = 5.203$, $b = 5.002$, $c = 5.018$ Å	$\alpha = \beta = \gamma = 90°$	$a = 5.154$, $b = 5.102$, $c = 5.104$ Å
o-AP	$a = 5.022$, $b = 9.944$, $c = 5.197$ Å	$\alpha = \beta = \gamma = 90°$	–
Monoclinic	$a = 5.092, b = 5.145, c = 5.261$ Å	$\alpha = \gamma = 90°, \beta = 99.83°$	$a = 5.117, b = 5.175, c = 5.291$ Å
			$\beta = 99.77°$ (Ref. [S4])

Analysis of the zone-center phonon modes calculated for different phases of HfO$_2$

In this section, we provide a detailed information of the calculated phonon frequencies along with their mode symmetry at the zone center for five studied phases of hafnia. We also provide a theoretical estimation of the longitudinal optic (LO) and transverse optic (TO) mode frequencies for all infrared-active modes. The TO mode frequencies were determined at the zone center $\mathbf{q} = \mathbf{0}$, whereas the LO mode frequencies were estimated at a nonzero wavevector $\mathbf{q_i} = \mathbf{0.001}\frac{2\pi}{\mathbf{a_i}}$ near the zone center, $\mathbf{a_i}$ being the real-space lattice vectors. We employ the Gonze scheme[S5,S6] as implemented in the PHONOPY package[S7] for non-analytical term correction. We note that, except for the cubic case, a strong mixing of the TO-mode eigenvectors occurs in the cases where more than one TO modes of the same symmetry are present, e.g., 8 infrared-active A$_1$ (TO) mode eigenvectors of o-III phase strongly mix on going from the TO to the LO case. Therefore, there is not a simple one-to-one correspondence between a LO mode and its associated TO mode in the tetragonal, o-III , o-AP , and monoclinic phases of hafnia. This is similar to the case of perovskite ferroelectrics.[S8]

Tables V, VI, VII, VIII, and IX contain the phonon frequencies calculated at the zone center (for TO modes) and near the zone center (for LO modes) for the cubic, tetragonal, o-III , o-AP , and monoclinic phases of pure hafnia, respectively.

1. Cubic phase ($Fm\bar{3}m$)

There are three atoms in the primitive unit cell of cubic hafnia. This results in a total of six optical phonon modes having following irreducible representation at the zone center

$$\Gamma_c = T_{2\mathrm{g}} \oplus T_{1\mathrm{u}}. \tag{1}$$

The triply degenerate $T_{2\mathrm{g}}$ (or Γ_5^+) modes are Raman active, whereas the triply degenerate $T_{1\mathrm{u}}$ (or Γ_4^-) modes are infrared active. The corresponding basis functions for the $T_{2\mathrm{g}}$ and $T_{1\mathrm{u}}$ modes are (xy, yz, zx) and (x, y, z), respectively.

Supplementary Table V. List of the calculated phonon frequencies for the cubic HfO_2

Modes	Frequency (cm^{-1})
T_{2g}	599
T_{1u} (TO)	266
T_{1u} (LO)	643

2. Tetragonal phase ($P4_2/nmc$)

The tetragonal unit cell of hafnia contains six atoms resulting in a total of 18 phonon modes, among which 15 modes are optical. The irreducible representations of the allowed optical phonon modes at the zone center are

$$\Gamma_t = 1\,A_{1\mathrm{g}} \oplus 2\,B_{1\mathrm{g}} \oplus 3\,E_{\mathrm{g}} \oplus 1\,A_{2\mathrm{u}} \oplus 1\,B_{2\mathrm{u}} \oplus 2\,E_{\mathrm{u}}. \tag{2}$$

The $A_{1\mathrm{g}}$ (or Γ_1^+), $B_{1\mathrm{g}}$ (or Γ_3^+), and E_{g} (or Γ_5^+) modes are Raman active, whereas $A_{2\mathrm{u}}$ (or Γ_2^-) and E_{u} (or Γ_5^-) modes are infrared active. The hyper-Raman $B_{2\mathrm{u}}$ (or Γ_4^-) mode is silent in typical Raman and infrared experiments. The corresponding basis functions for the Raman active modes $A_{1\mathrm{g}}$, $B_{1\mathrm{g}}$, and E_{g} are $(x^2 + y^2, z^2)$, $(x^2 - y^2)$, and (xz, yz), respectively, and the basis functions for the infrared-active modes $A_{2\mathrm{u}}$ and E_{u} are (z) and (x, y), respectively. The $A_{2\mathrm{u}}$ mode has the strongest polar nature in this system, and it is responsible for generating polarization along the z direction.

Supplementary Table VI. List of the calculated phonon frequencies for the tetragonal HfO_2

Modes	Frequency (cm^{-1})
1 A_{1g}	276
2 B_{1g}	240, and 609
3 E_g	107, 474, and 677
1 A_{2u} (TO)	321
1 A_{2u} (LO)	633
1 B_{2u}	682
2 E_u (TO)	129, and 460
2 E_u (LO)	267, and 711

3. *o-III* **phase** ($Pca2_1$)

The unit cell of the orthorhombic polar phase (*o-III*) of hafnia contains twelve atoms resulting in a total of 36 phonon modes, among which 33 modes are optical, as listed in Table VII. The irreducible representations of the allowed optical phonon modes at the zone center are:

$$\Gamma_{o\text{-}III} = 8\,A_1 \oplus 9\,A_2 \oplus 8\,B_1 \oplus 8\,B_2. \tag{3}$$

All the optical phonons are Raman active, whereas only A_1, B_1, and B_2 are infrared active. The corresponding basis functions for the A_1 (or Γ_1), A_2 (or Γ_3), B_1 (or Γ_2), and B_2 (or Γ_4) modes are (z, x^2, y^2, z^2), (xy), (x, xz), and (y, yz), respectively. The infrared active A_1, B_1, and B_2 modes generate polarization along the z, x, and y directions, respectively. Therefore, the LO splitting of the respective A_1(TO), B_1(TO), and B_2(TO) modes occurs along the q_z, q_x, and q_y directions in the reciprocal space, respectively.

4. *o-AP* **phase** ($Pbca$)

The orthorhombic antipolar phase (*o-AP*) of hafnia contains 24 atoms/cell resulting in a total of 72 phonon modes, among which 69 modes are optical, as listed in Table VIII. The

Supplementary Table VII. List of the calculated phonon frequencies for the *o-III* HfO$_2$

Modes	Frequency (cm^{-1})
8 A$_1$ (TO)	126, 167, 261, 340, 354, 396, 471, and 607
8 A$_1$ (LO)	129, 189, 264, 340, 395, 439, 595, and 677
9 A$_2$	129, 143, 155, 309, 417, 492, 589, 664, and 696
8 B$_1$ (TO)	130, 244, 276, 345, 397, 497, 643, and 702
8 B$_1$ (LO)	131, 310, 349, 349, 492, 615, 690, and 724
8 B$_2$ (TO)	144, 244, 252, 342, 403, 532, 562, and 747
8 B$_2$ (LO)	146, 251, 306, 345, 511, 560, 651, and 797

irreducible representations of the allowed optical phonon modes at the zone center are

$$\Gamma_{o\text{-}AP} = 9\,A_{\mathrm{g}} \oplus 9\,B_{1\mathrm{g}} \oplus 9\,B_{2\mathrm{g}} \oplus 9\,B_{3\mathrm{g}} \oplus 9\,A_{\mathrm{u}} \oplus 8\,B_{1\mathrm{u}} \oplus 8\,B_{2\mathrm{u}} \oplus 8\,B_{3\mathrm{u}}. \tag{4}$$

The A_{g} (Γ_1^+), $B_{1\mathrm{g}}$ (Γ_3^+), $B_{2\mathrm{g}}$ (Γ_2^+), and $B_{3\mathrm{g}}$ (Γ_4^+) modes are Raman active, whereas $B_{1\mathrm{u}}$ (Γ_3^-), $B_{2\mathrm{u}}$ (Γ_2^-), and $B_{3\mathrm{u}}$ (Γ_4^-) modes are infrared active. The A_{u} (Γ_1^-) modes are silent in typical Raman and infrared measurements. The basis functions for the Raman-active modes A_{g}, $B_{1\mathrm{g}}$, $B_{2\mathrm{g}}$, and $B_{3\mathrm{g}}$ are (x^2, y^2, z^2), (xy), (zx), and (yz), respectively. The basis functions for the IR-active modes $B_{1\mathrm{u}}$, $B_{2\mathrm{u}}$, and $B_{3\mathrm{u}}$ are z, y, and x, respectively.

5. Monoclinic phase ($P2_1/c$)

The monoclinic unit cell of hafnia contains 12 atoms/cell resulting in 33 optical phonon modes. The irreducible representations of the allowed optical phonon modes at the zone center are

$$\Gamma_m = 9\,A_{\mathrm{g}} \oplus 9\,B_{\mathrm{g}} \oplus 8\,A_{\mathrm{u}} \oplus 7\,B_{\mathrm{u}}. \tag{5}$$

All the A_{g} (or Γ_1^+) and B_{g} (or Γ_2^+) modes are Raman active, whereas all the A_{u} (or Γ_1^-) and B_{u} (or Γ_2^-) modes are infrared active. The corresponding basis functions for the Raman active modes A_{g} and B_{g} are (x^2, y^2, z^2, xz) and (xy, yz), respectively, and the basis functions for the infrared-active modes A_{u} and B_{u} are (y) and (x, z), respectively.

Supplementary Table VIII. List of the calculated phonon frequencies for the *o-AP* HfO_2

Modes	Frequency (cm^{-1})
9 A_g	113, 139, 200, 260, 334, 380, 438, 575, and 626
9 B_{1g}	143, 173, 198, 312, 341, 465, 505, 585, and 793
9 B_{2g}	113, 133, 252, 259, 349, 501, 577, 622, and 710
9 B_{3g}	130, 161, 220, 310, 442, 470, 585, 663, and 701
9 A_u	92, 138, 152, 311, 386, 434, 521, 586, and 740
8 B_{1u} (TO)	129, 190, 276, 390, 421, 485, 622, and 698
8 B_{1u} (LO)	190, 311, 313, 415, 477, 600, 683, and 730
8 B_{2u} (TO)	82, 248, 261, 354, 385, 408, 532, and 739
8 B_{2u} (LO)	83, 249, 317, 355, 408, 502, 643, and 793
8 B_{3u} (TO)	187, 201, 223, 355, 365, 420, 578, and 654
8 B_{3u} (LO)	193, 207, 232, 356, 413, 556, 653, and 671

Supplementary Table IX. List of the calculated phonon frequencies for the monoclinic HfO_2

Modes	Frequency (cm^{-1})
9 A_g	117, 135, 147, 259, 340, 392, 500, 576, and 668
9 B_g	132, 168, 247, 330, 406, 518, 550, 634, and 780
8 A_u (TO)	134.1, 185, 256, 362, 415, 508, 607, and 661
8 A_u (LO)	134.2, 186, 276, 390, 481, 572, 661, and 749
7 B_u (TO)	240, 255, 330, 345, 403, 518, and 741
7 B_u (LO)	254, 270, 340, 370, 511, 655, and 802

———

[S1] Okhotnikov, K., Charpentier, T. & Cadars, S. Supercell program: a combinatorial structure-generation approach for the local-level modeling of atomic substitutions and partial occupancies in crystals. *Journal of Cheminformatics* **8**, 17 (2016). URL https://doi.org/10.1186/s13321-016-0129-3.

[S2] Zhao, X. & Vanderbilt, D. First-principles study of structural, vibrational, and lattice dielectric

properties of hafnium oxide. *Phys. Rev. B* **65**, 233106 (2002). URL `https://link.aps.org/doi/10.1103/PhysRevB.65.233106`.

[S3] Wang, J., Li, H. P. & Stevens, R. Hafnia and hafnia-toughened ceramics. *Journal of Materials Science* **27**, 5397–5430 (1992). URL `https://doi.org/10.1007/BF00541601`.

[S4] Adam, J. & Rogers, M. D. The crystal structure of ZrO_2 and HfO_2. *Acta Crystallographica* **12**, 951–951 (1959). URL `https://onlinelibrary.wiley.com/doi/abs/10.1107/S0365110X59002742`.

[S5] Gonze, X., Charlier, J.-C., Allan, D. & Teter, M. Interatomic force constants from first principles: The case of α-quartz. *Phys. Rev. B* **50**, 13035–13038 (1994). URL `https://link.aps.org/doi/10.1103/PhysRevB.50.13035`.

[S6] Gonze, X. & Lee, C. Dynamical matrices, Born effective charges, dielectric permittivity tensors, and interatomic force constants from density-functional perturbation theory. *Phys. Rev. B* **55**, 10355–10368 (1997). URL `https://link.aps.org/doi/10.1103/PhysRevB.55.10355`.

[S7] Togo, A. & Tanaka, I. First principles phonon calculations in materials science. *Scr. Mater.* **108**, 1–5 (2015). URL `https://doi.org/10.1016/j.scriptamat.2015.07.021`.

[S8] Zhong, W., King-Smith, R. D. & Vanderbilt, D. Giant LO-TO splittings in perovskite ferroelectrics. *Phys. Rev. Lett.* **72**, 3618–3621 (1994). URL `https://link.aps.org/doi/10.1103/PhysRevLett.72.3618`.